nature communications

Article

https://doi.org/10.1038/s41467-024-55109-w

# Photoswitch dissociation from a G protein-coupled receptor resolved by time-resolved serial crystallography

Received: 20 March 2024

Accepted: 27 November 2024

Published online: 30 December 2024

Check for updates

Hannah Glover[1], Torben Saßmannshausen[2], Quentin Bertrand[1], Matilde Trabuco[3], Chavdar Slavov[2,4], Arianna Bacchin[3], Fabio Andres[3], Yasushi Kondo[1], Robin Stipp[1], Maximilian Wranik[1], Georgii Khusainov[1], Melissa Carrillo[1], Demet Kekilli[1], Jie Nan[5], Ana Gonzalez[5], Robert Cheng[3], Werner Neidhart[3], Tobias Weinert[1], Filip Leonarski[6], Florian Dworkowski[6], Michal Kepa[1], Josef Wachtveitl[2], Michael Hennig[3] & Joerg Standfuss[1]

G protein-coupled receptors (GPCRs) are the largest family of cell surface receptors in humans. The binding and dissociation of ligands tunes the inherent conformational flexibility of these important drug targets towards distinct functional states. Here we show how to trigger and resolve protein-ligand interaction dynamics within the human adenosine $A_{2A}$ receptor. For this, we designed seven photochemical affinity switches derived from the anti-Parkinson's drug istradefylline. In a rational approach based on UV/Vis spectroscopy, time-resolved absorption spectroscopy, differential scanning fluorimetry and cryo-crystallography, we identified compounds suitable for time-resolved serial crystallography. Our analysis of millisecond-scale dynamics revealed how trans-to-cis isomerization shifts selected istradefylline derivatives within the binding pocket. Depending on the chemical nature of the ligand, interactions between extracellular loops 2 and 3, acting as a lid on the binding pocket, are disrupted and rearrangement of the orthosteric binding pocket is invoked upon ligand dissociation. This innovative approach provides insights into GPCR dynamics at the atomic level, offering potential for developing novel pharmaceuticals.

Time-resolved serial crystallography (TRSX) is a method to investigate dynamic processes experimentally at near-atomic resolution. In the most common form of TRSX, protein crystals at room temperature are first 'pumped' by a trigger and then 'probed' by X-rays, allowing for the synchronous initiation of reactions and determination of the structures of intermediates along the reaction pathway. Although a variety of trigger systems have been used[1], optical activation is the most common due to the relative simplicity of its experimental setup, its efficiency and the speed with which activation occurs. As a result, membrane proteins containing endogenous photoswitches have been the focus of TRSX studies[2–4]. However, since only a small minority of proteins are naturally photosensitive[5], photoswitchable substitutes of ligands need to be found to ensure that this method can be applied to a wider variety of systems.

One potential solution to this problem arises from the field of photopharmacology, which focuses on the design of synthetic photoswitches to improve the spatial and temporal control of drug delivery in patients[6]. Light-driven isomerization, as occurring in

[1]PSI Center for Life Sciences, Villigen PSI, Switzerland. [2]Institute of Physical and Theoretical Chemistry, Goethe University, Frankfurt, Germany. [3]leadXpro AG, Park Innovaare, Villigen PSI, Switzerland. [4]Department of Chemistry, University of South Florida, Tampa, USA. [5]MaxIV Laboratory, Lund University, Lund, Sweden. [6]PSI Center for Photon Sciences, Villigen PSI, Switzerland. e-mail: joerg.standfuss@psi.ch

azobenzenes and stilbenes, has frequently been used to achieve large changes in geometry that reversibly switches a ligand between low- and high-affinity states[7]. Such photochemical affinity switches have been developed for a wide variety of non-endogenously photoactive proteins and have been characterized for their photopharmacological properties[8–10]. In recent work, we have demonstrated the use of the prototypical photoswitch azo-combretastatin A4 to study the dynamics of ligand dissociation from tubulin in the femto–to–millisecond range[11–13]. Structural details of how low- and high-affinity variants of the same ligand interact with the binding pocket can help with identification of key regions contributing to biological activity. Resolving the structural dynamics of ligand-protein interactions may have further implications for understanding the molecular mechanisms of drug actions or the design of better drugs, for example, by optimizing $k_{off}$ with knowledge of the dissociation pathway. It is therefore of great scientific interest to expand the application of synthetic photoswitches in TRSX to other protein targets.

While employing photochemistry to enable the light control of non-photoreactive proteins has many applications[10,14–16], there are currently no clear guidelines for the design and selection of synthetic photoswitches to enable time-resolved studies by TRSX. Additionally, there is often a discrepancy in the characterization of properties in photopharmacology and the conditions that would be needed for TRSX. In photopharmacology, spectroscopic characterizations typically use continuous long-term illumination in the absence of protein, allowing low quantum yields to be overcome[9,17]. However, TRSX studies may require isomerization to occur efficiently within the protein binding pocket using only a short photon pulse to not limit the achievable temporal resolution. This discrepancy has already been noted for photocaged molecules for use in TRSX[5].

To test the design and selection of a photoswitch for TRSX with a pharmacologically relevant protein, we selected the human adenosine $A_{2A}$ receptor ($A_{2A}R$). The $A_{2A}R$ is a prominent member of the G protein-coupled receptor family of proteins (GPCRs), which transmit biological signals across cellular membranes. Like many GPCRs, there is a lack of photoswitches to target the $A_{2A}R$, though a novel photoswitchable agonist[18] and the application of the antagonist istradefylline in photopharmacology[17] have been recently described.

Ligand induced conformational changes are critical to this function, as they promote the interaction of GPCRs with their intracellular binding partners. The development of small molecule drugs that mimic natural ligands to modulate GPCR activity is a classical form of medical intervention[19]. Because of the fundamental biological relevance and complex pharmacology of GPCRs, a wide range of biophysical, structural, and cell biology techniques have been employed to reveal how structural dynamics underlying receptor function are modulated by ligand binding[20–25]. These studies have enforced the reliance of receptor function on protein flexibility, both on the scale of side chain movements in the binding pocket and the changes following receptor activation.

In addition to being known as the receptor responsible for the effects of caffeine[26], the $A_{2A}R$ also plays an important role in the regulation of dopamine signaling to help control motor function in the basal ganglia[27,28]. This function highlighted the $A_{2A}R$ as a target for the treatment of Parkinson's disease and prompted development of the anti-Parkinson's drug istradefylline[29,30]. The $A_{2A}R$ was selected as a good test case for the application of synthetic photoswitches to study GPCRs using TRSX as it has been extensively studied, being one of the first GPCRs with structures solved in antagonist[31] and agonist bound conformations, with[32] and without[33] G protein binding.

Here, we designed photoswitch candidates to study binding pocket dynamics in the human $A_{2A}R$. We evaluated them first by cryo-crystallography and a combination of biophysical techniques, including differential scanning fluorimetry, standard UV/Vis spectroscopy and transient absorption spectroscopy. The best compounds where then used for serial crystallography experiments to shed light on how small chemical modifications can change binding characteristics after light illumination. Based on these findings, we carried out a time-resolved study with millisecond time resolution, showing isomerization and release of this photoswitch. While ligand design will always be very specific to the target and starting point, our defined criteria, careful characterization and selection of ligands for TRSX experiments can serve as a general framework enabling time-resolved crystallographic studies on non-photoswitchable proteins without a category of established photoswitches.

## Results and discussion

Given its relevance as a Parkinson's drug, and structural similarity to the endogenous ligand caffeine, we chose the $A_{2A}R$ antagonist istradefylline as the starting point for photoswitch development (Fig. 1). Istradefylline is known to be photosensitive through photoisomerization around its central stilbene bond[34–36], and has recently been used as an optical control of $A_{2A}R$ signaling in zebrafish[17]. However, the low solubility of istradefylline prevented reproducible crystallization, making it unsuitable for TRSX studies. We therefore designed and selected a series of istradefylline variants (StilSwitch1-4) with the aim of improving both solubility and photoisomerization efficiency, which are key to obtaining TRSX datasets with sufficient signal to observe conformational changes. The removal of methyl groups from various points of istradefylline, such that a hydrogen bond donor or acceptor is revealed, can increase solubility. This modification will also alter the electronic properties of the molecules, helping to influence the photoisomerization kinetics. Many derivatives of istradefylline involving this modification are commercially available. This type of modification was also chosen so as not to introduce bulky groups, which could interfere with the interactions of the ligand and residues of the binding pocket. For xanthine-based antagonists of the $A_{2A}R$, such as istradefylline, this is a hydrogen bond with $N253^{6.55}$ (superscripts refer to Ballesteros-Weinstein numbering[37]) and aromatic ring stacking with $F168^{ECL2}$. Following isomerization, these interactions are still possible; however, clashes at the top of the binding pocket with the isomerized photoswitch will decrease the overall favorability of binding and decrease ligand affinity. Other investigated modifications involved replacement of the central C=C stilbene bridge with an N=N azobenzene bond (AzoSwitch1-3), as azobenzenes are known to have more efficient isomerization than stilbenes and absorb at longer wavelengths[38], properties that made them prototypical photoswitches for many applications[10,15,16].

We formulated three key properties to enable successful TRSX experiments using designed photoswitches, (Fig. 1); (I) the bound ligand structure can be obtained (a convolution of solubility, crystallization conditions and affinity); (II) a detectable effect of photoswitching on the protein and (III) efficient photoisomerization in the protein binding pocket (which can significantly differ from solution). Based on these properties, candidates from a pool of commercially available and custom synthesized istradefylline derivatives were evaluated through cryo-crystallography and a series of biophysical assays, which provided a basis for deciding whether to continue a photoswitch candidate through the characterization pipeline.

### Crystallographic characterization of photoswitches

Prior to biophysical characterization of the istradefylline derivatives, crystal structures were obtained to ensure modifications to the ligand did not prevent binding in the orthosteric pocket. This also enabled solubility for crystallization to be assessed, a key parameter which prevented the use of istradefylline as a photoswitch for TRSX. AzoSwitch1 and AzoSwitch3 were ruled out from further characterization, due to their low solubility causing precipitation of the compounds, even at higher solvent concentrations in the soaking buffer. Crystals

https://doi.org/10.1038/s41467-024-55109-w

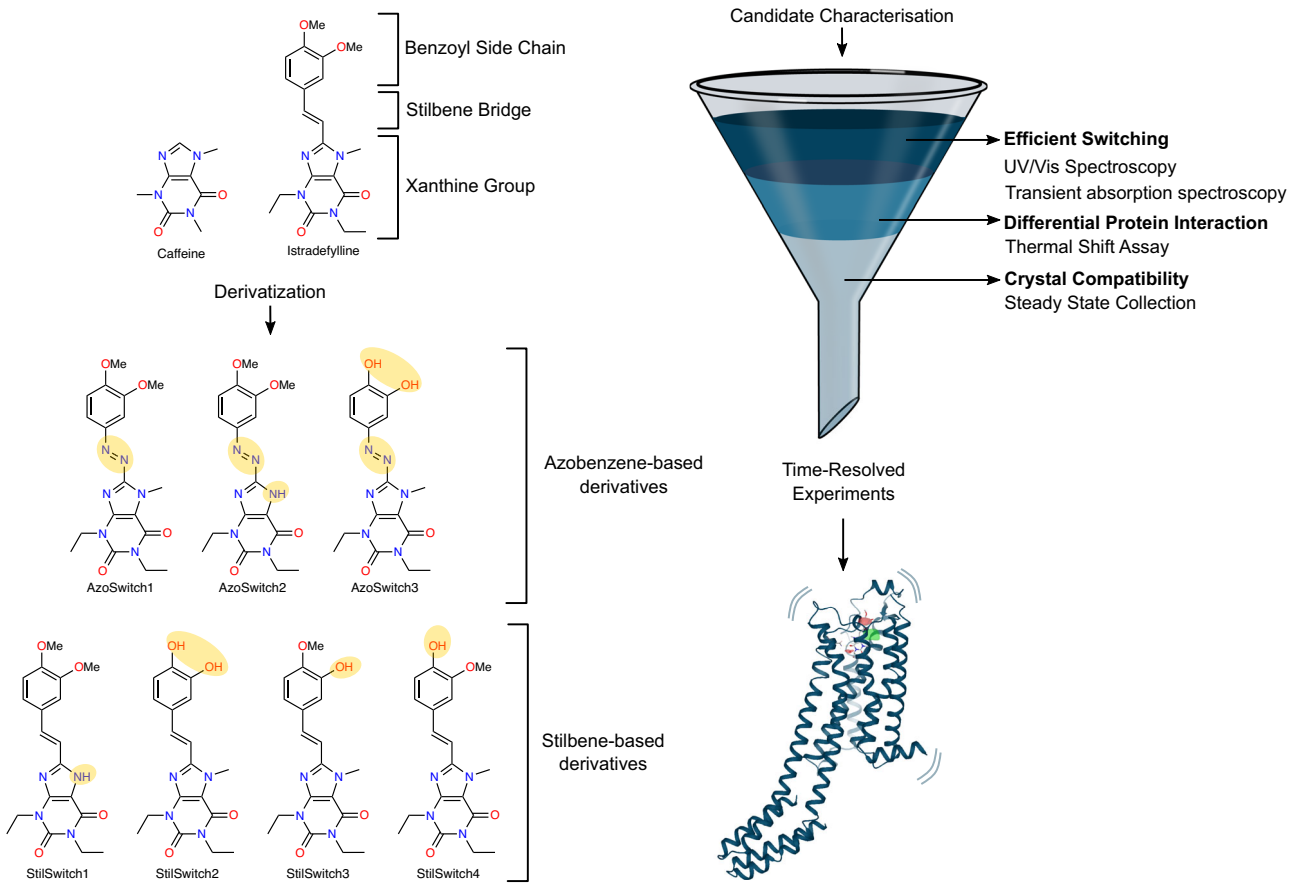


**Fig. 1 | Design and selection of synthetic photoswitches.** Derivatives were made through modifying the three basic building blocks of istradefylline: the xanthine group, the stilbene bridge, and the benzoyl side chain. Positions at which modifications were made are highlighted in yellow. These derivatives were subject to experimental characterization with three main properties deemed as important for time-resolved serial crystallography.

soaked with the remaining ligands diffracted to resolutions of 1.95–2.35 Å (Supplementary Table 1), allowing the binding interactions of the ligands to be clearly identified and demonstrating that modification of the istradefylline scaffold did not prevent ligand binding (Fig. 2 and Supplementary Fig. 1). The binding pose was similar for all photoswitches and is typical of xanthine-based antagonists of the $A_{2A}R$[39]. Additionally, some derivatives formed water-mediated hydrogen bonds with the carbonyl group of $S67^{2.65}$. All ligands also interacted with $E169^{ECL2}$, either through π-hydrogen bonds or water-mediated hydrogen bonds. $E169^{ECL2}$ forms part of a lid over the $A_{2A}R$ binding pocket[40] together with $T256^{6.58}$ and $H264^{ECL3}$. Previous studies have demonstrated that stabilization of the ionic interaction between $E169^{ECL2}$ and $H264^{ECL3}$ through ligand interactions can produce longer residence times[41]. Therefore, the removal of this stabilization after isomerization is likely to cause a reduction in affinity through the modification of dissociation kinetics. The inhibition constant of *cis* istradefylline has previously been measured and was observed to be lower than that of the *trans* state[36], supporting the idea that the *cis* states of the istradefylline derivatives are likely to have lower affinities.

## Assessing the effect of photoswitching on the protein

A photoswitch designed for use in TRSX must detectably change the protein-ligand interaction to induce conformational changes upon illumination. As it is well known that GPCRs are stabilized by the binding of high-affinity ligands[42], we used changes in thermal stability to assess the magnitude of changes in protein-ligand interactions. A simple method available in most labs for studying these changes is differential scanning fluorimetry, which takes advantage of fluorescent dyes to monitor the temperature-induced unfolding of proteins[43]. For all investigated photoswitches, we observed a progression of the melting curve from the dark bound state back towards the apo state upon illumination: both in terms of melting temperature and the rate of onset of the melting transition (Fig. 3A). The reduction in thermal shift of illuminated relative to dark samples demonstrates that illumination causes a decrease in the thermal stabilization of the $A_{2A}R$ by the photoswitch, which can be interpreted to correlate approximately with photoswitch affinity.

Whilst monitoring thermal shifts is a simple method to assess changes in the global protein-ligand interactions in solution, it is not well suited to assessing temporal changes occurring over short timescales. This assay instead provides a clear picture of the state of the thermodynamic equilibrium the protein reaches after illumination of varying amounts of time. Using long illumination timescales, photoswitches undergo many successive photocycles; gradually increasing the proportion of molecules in the low-affinity state until a photostationary state is reached. However, in the case of stilbene-based photoswitches, photocycloaddition reactions take place that permanently lock the photoswitches in non-binding state[17]. This results in the lack of a photostationary state and the progressive increase in proportion of molecules in the low affinity state. Allowing differences in the protein stabilization at different proportions of *trans* and *cis* photoswitch to be observed. Characterization of the ratio of photoswitch in a high- and low-affinity state after different illumination times using, for example, NMR spectroscopy could be used in combination with differential scanning fluorimetry to more accurately analyze data from this method and to allow extrapolation of data to the fully isomerized state. However, these techniques are not always easily accessible and for

https://doi.org/10.1038/s41467-024-55109-w

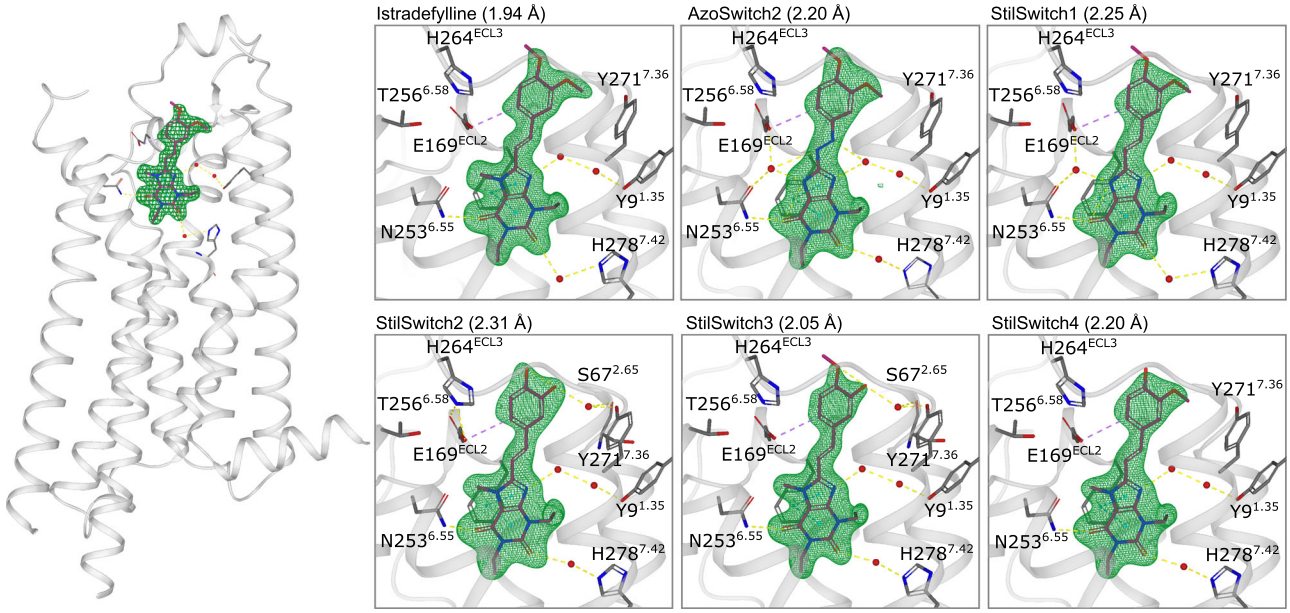


**Fig. 2 | Binding poses of istradefylline and five of its derivatives in the $A_{2A}$ binding pocket.** The $F_o$-$F_o$ omit maps are carved around the ligands and contoured at 3.0 sigma. Density of the omit maps indicates full replacement of theophylline by the photoswitches in the binding pocket.

selection of best candidates from a pool, relative performance is sufficient.

The impact of the derivatization of istradefylline on the change in thermal shift can be observed clearly for StilSwitch2-4, all of which have modifications reducing the size of the benzoyl ring relative to istradefylline. The smaller the size of the benzoyl ring, the slower the rate of thermal shift decrease after illumination: indicating that this moiety must be instrumental in determining the lower affinity of the *cis* state through changing the interactions of the ligand with the binding pocket.

## Isomerization efficiency characterization

TRSX requires a high level of photoactivation to visualize signals in isomorphous difference maps. Photoswitch isomerization efficiencies are typically measured in the absence of protein. However, the influence of the local confinement in the binding pocket on isomerization efficiency also needs to be taken into consideration. To determine relative photoisomerization efficiencies, the absorption spectra were measured using UV/Vis spectroscopy before and after 1 min of constant illumination in the presence and absence of protein (Fig. 3B). A larger decrease in *trans* peak absorbance following illumination would be characteristic of a higher efficiency of photoconversion. Protein binding lowered the efficiency for all isomerizing ligands, supporting previous conclusions that protein binding can reduce the quantum efficiency of photoisomerization[44]. Interestingly, only small changes were observed for AzoSwitch2, despite azobenzenes typically isomerizing with a higher efficiency than stilbenes[38]. This observation was later shown to be due to a short half-life of the *cis* state, resulting in thermal relaxation back to the *trans* state before measurement (Supplementary Fig. 2), revealing the importance of kinetic ligand characterization already at this point.

Three derivatives had higher isomerization efficiencies than istradefylline in the protein-bound state: StilSwitch2, StilSwitch3, and StilSwitch4. Comparing the size of the benzoyl moiety, the group with the strongest influence on *cis* state affinity, with the effect protein binding has on photoisomerization efficiency (Supplementary Fig. 3), it is clear that reducing the size of the photoswitch improves photoisomerization when bound to the protein. Whilst increasing the probability of *cis* state formation was a desired property, when comparing the results of UV/Vis spectroscopy to differential scanning fluorimetry, it is clear that this increase in *cis* state formation came at the expense of eliciting large changes in protein interactions following isomerization due to the reduction in clashes formed with the binding pocket. Together, these results demonstrate that isomerization efficiency alone should not be used to select photoswitches for use in TRSX. Instead, photoswitches should have a balance of high-yielding isomerization in the protein binding pocket, and large differences in protein-ligand interactions following isomerization. StilSwitch3 and StilSwitch4 balance these effects, given that their isomerization efficiency is not dramatically reduced by protein binding, photoswitching occurs with good yields, and the total decrease in thermal shift following illumination was the largest for these photoswitches.

## Kinetic characterization of photoswitch candidates

A time-resolved spectroscopic characterization of the photoswitch derivatives was carried out to probe isomerization dynamics in more detail. Transient absorption spectroscopy shows that at around 10 ps, the stilbene-based photoswitches exhibit an additional state in aqueous solution (Fig. 4E, F), which was not observed in acetonitrile (Supplementary Fig. 5). The intensity of the new state scales in the order StilSwitch1 <StilSwitch3 <StilSwitch4 <StilSwitch2, also visible in the normalized transients (Fig. 4E). Here, we see a rising intensity around 10 ps associated with this state. Time needed for populations of the additional state follows the same order as the intensity. StilSwitch3 shows the highest remaining signal, while StilSwitch1 shows the lowest isomerization yield (Fig. 4E, F). This result resembles the steady-state spectra when illuminating at 340 nm. Remarkably, StilSwitch2 and StilSwitch4 (highest novel state concentration) show red-shifted steady-state fluorescence spectra (Supplementary Fig. 4F), indicating another radiating species. Based on this analysis, an excited state branching is likely. One part of the excited population undergoes isomerization, while the second part most likely forms a conformationally relaxed intramolecular charge transfer (CRICT) state. This state is well known for push-pull-stilbenes and decays via fluorescence[45–49].

Looking into the kinetics of the photoreaction of StilSwitch3 (Fig. 4A), we observe a broad excited state absorption, extending out to 100 ps. The stimulated emission (405–450 nm) overlaps with the

https://doi.org/10.1038/s41467-024-55109-w

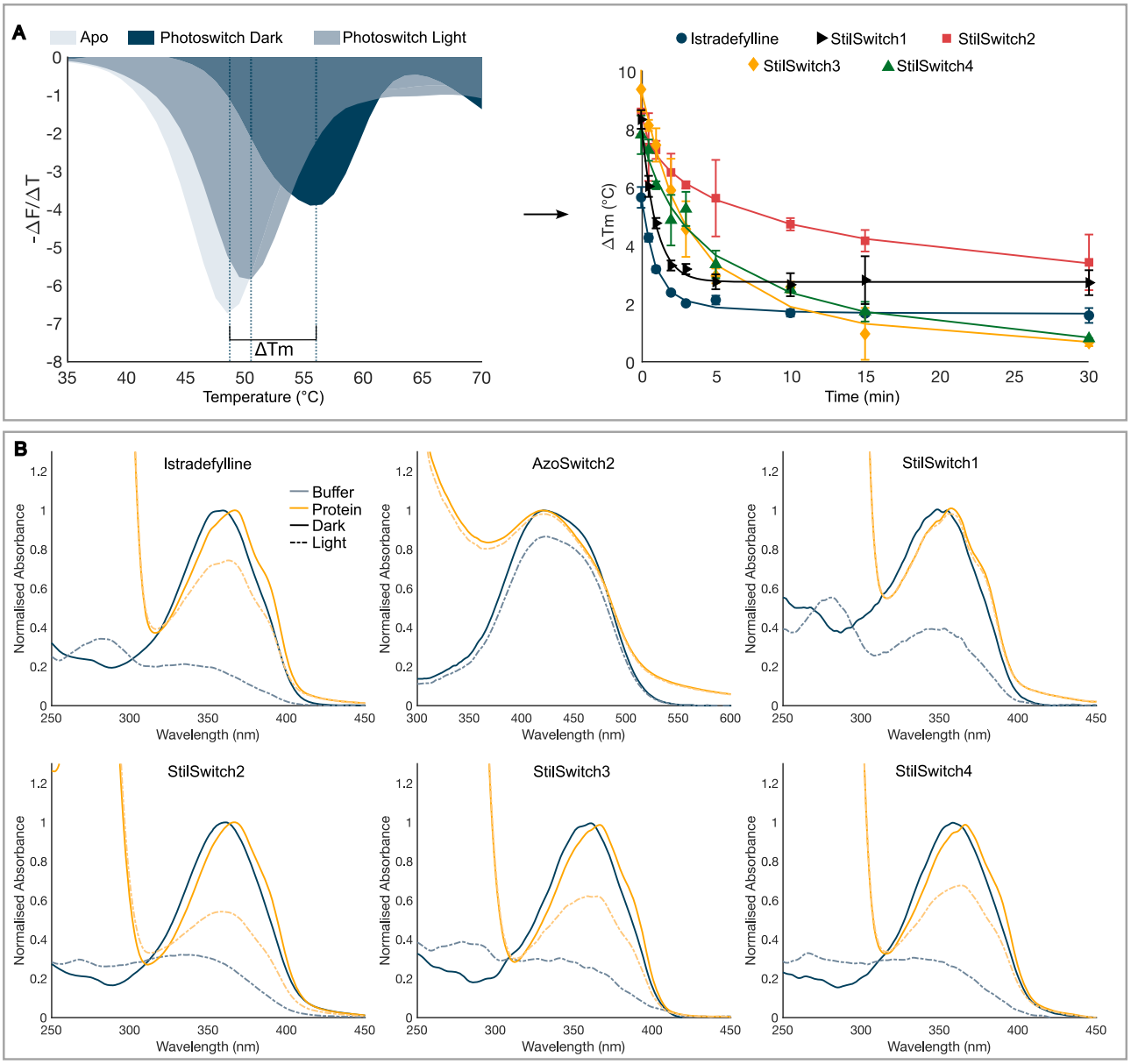


**Fig. 3 | Biophysical characterization of photoswitch candidates. A** Differential scanning fluorimetry of photoswitches. The first derivative of the fluorescence curves (left) displays a progression of photoswitch-bound curves towards the apo curve after illumination. Increasing the illumination time (right) results in a progressive decrease in the melting temperature for all photoswitches: istradefylline, blue circles; StilSwitch1, black rightward triangles; StilSwitch2, red squares; StilSwitch3, yellow diamonds; StilSwitch4, green upwards triangles. Data are displayed as mean values ± the confidence interval calculated at 0.05 significance. Technical replicates were collected for each data point throughout multiple experiments using aliquots of the same protein sample. The number of replicates for each data point and the calculated confidence intervals are detailed in the source data file. The change in thermal shifts (ΔΔTm) of the photoswitches are: Istradefylline −4.04 °C, Switch2 −5.15 °C, Switch3 −8.67 °C, Switch4 −6.98 °C. **B** UV/Vis Absorption Spectra of photoswitches absorption under dark (solid line) and illuminated (dashed line) conditions in buffer (blue) and bond to the protein (yellow). All stilbene-derivatives display a ~6 nm shift in the trans absorption peak after protein binding. Source data are provided as a source data file.

CRICT state while the ground state bleach (<400 nm) signal is constant at 2 ns, indicating successful isomerization. The lifetime density analysis yields four different lifetime distributions at 1 ps, 4 ps, 40 ps, and >2 ns (Fig. 4B). While the first density accounts for excited state absorption (ESA) and the decay of stimulated emission (SE) and consequently partial ground state bleach (GSB) recovery, the second, negative distribution accounts for formation of the CRICT state. Within the third component, the ESA and the CRICT state decay, while the last distribution indicates product formation. Within the constraining protein, the decay of StilSwitch3 is slowed (Fig. 4C, D) and the CRICT state formation is no longer visible. To obtain the key populations and states involved in the photoreaction, we performed a global target analysis with a sequential model (Fig. 4G). The best fits were achieved with four different lifetimes. The corresponding evolution-associated difference spectra (Supplementary Fig. 5A) show the involved states and have very common spectral features, only the intensities vary. This supports the idea of a strongly decreased photoreaction (Supplementary Fig. 6B) combined with a strongly non-exponential behavior. Remarkably, the CRICT state formation is inhibited by the protein environment, which prevents this inactivation pathway. On the other hand, the isomerization rate is also slowed down and reduced by the protein environment. Since the photoreaction proceeds beyond the measurement time window, we cannot observe complete isomerization here, however, the steady-state data

https://doi.org/10.1038/s41467-024-55109-w

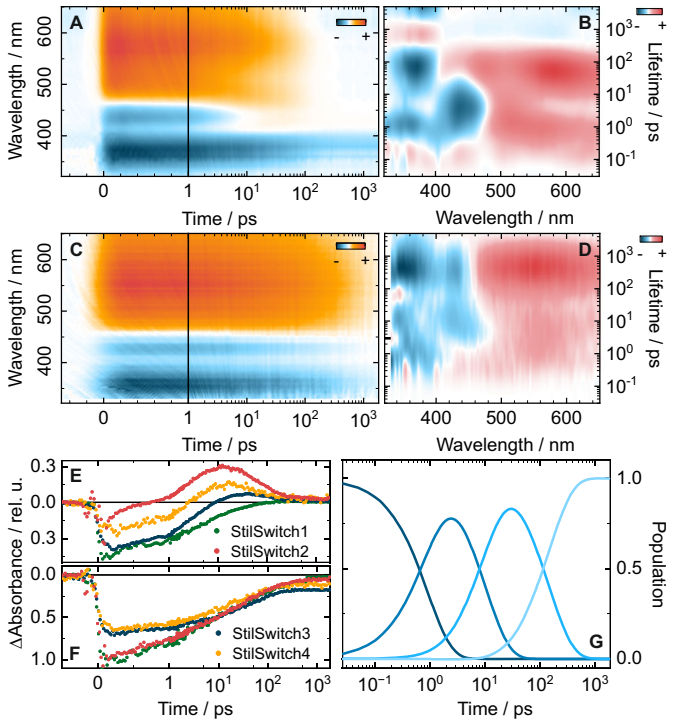


**Fig. 4 | Photoswitch kinetics probed by transient absorption spectroscopy.** **A**–**D**: Transient absorption data of Switch3 in buffer (**A**) and with protein (**C**) on the left and the corresponding Lifetime Density Maps (LDM) on the right (**B**, **D**). For the transient data, positive signals indicate a product absorption (PA) or an excited state absorption (ESA), the negative signals refer to ground state bleach (GSB) or stimulated emission (SE). In the LDMs the positive components describe a rising negative or a decaying positive signal. The negative component depicts a decaying negative or a rising positive signal. In (**E**, **F**) normalized transients of Switch14 are displayed. The transients are normalized to the highest ESA signal in the dataset and show the maximum SE and remaining GSB signal, respectively. **G** shows the populations obtained from global target analysis for Switch3 bound to protein. Source data are provided as a source data file.

(Fig. 3B) demonstrate a *trans* to *cis* photoreaction. In combination with the steady-state data, it can be concluded that the process has lower rates and lower quantum yields within the protein binding pocket, as is often the case for photoswitches under confined conditions[44,50–53]. Overall StilSwitch3 showed the highest photoconversion in the steady state, while having only a very small formation of the non-productive CRICT state, suggesting it as an ideal candidate to test its photoreaction when bound to the $A_{2A}R$.

## Assessing behavior of photoswitches *in crystallo* with serial crystallography

After balancing characteristics of the designed istradefylline derivatives (Supplementary Fig. 7), we selected StilSwitches2-4 as promising candidates for serial synchrotron crystallographic experiments. Following protocols, we developed for the study of light-activated rhodopsins[11,54–56], we collected serial crystallographic datasets under constant illumination at the Swiss Light Source. In the case of StilSwitch4, crystals did not yield sufficient diffraction patterns under these conditions. Also, in the case of StilSwitch2 and StilSwitch3, light exposure reduced the rate at which diffraction patterns could be collected. Nevertheless, crystals diffracted well enough for the collection of light-activated datasets (Supplementary Table 2) with resolutions of 2.80 Å and 3.05 Å, respectively.

Difference electron density maps and structural refinements against the data show clear *trans-cis* isomerization around the stilbene C=C double bond (Fig. 5A, B). Following isomerization, the xanthine-base of the photoswitches undergoes a slight shift in position, still allowing the interactions with $N253^{6.55}$ and $F168^{ECL2}$ to take place, but at a less optimal distance than compared to the dark state. The movement of the xanthine base away from its dark state position is likely driven by clashes formed between the protein and the benzoyl side chain of the photoswitches. Even though both ligands only differ by a single methyl group on the tilting benzoyl side chain, the photo-induced change had somewhat unexpectedly different effects on the ligand binding pocket. Of particular interest in this regard is the hydrogen bond network formed by the triad of $E169^{ECL2}$, $T256^{6.58}$, and $H264^{ECL3}$ and the hydrophobic pocket above $Y271^{7.36}$ that have been suggested as key sites during multistep ligand dissociation in the $A_{2A}R$ based on mutagenesis and molecular dynamic simulations[40].

In the case of both StilSwitch2 and StilSwitch3 the resulting *cis*-state clashes with $Y271^{7.36}$ and causes it to move away from the binding pocket (Fig. 5A, B). In StilSwitch2 these changes shift the position of the hydrogen-bonded lid on the binding pocket ($E169^{ECL2}$, $H264^{ECL3}$, $T256^{6.58}$) without opening it. Key features of the *cis* state-bound binding pocket observed with StilSwitch2 are also present for StilSwitch3. However, the clash with $Y271^{7.36}$ at the base of ECL3 is more pronounced, likely because the extra methyl group increases the size of the benzoyl moiety. These changes partially break the hydrogen bond between $H264^{ECL3}$ and $E169^{ECL2}$ opening the suggested exit pathway between ECL2 and ECL3 (Fig. 5B, D–F)[40]. These structural results explain the larger change in thermal shift upon illumination of StilSwitch3 and suggests that the extra methyl group on the benzoyl ring changes dissociation kinetics. This difference potentially allowed us to trap two different intermediates of the dissociation pathway, further emphasized by a shift in the sodium ion, known to modulate $A_{2A}R$ activity and ligand binding[57,58], only observed in StilSwitch3 (Fig. 5C). Cholesterol is another allosteric regulator of $A_{2A}R$ activity with state-dependent binding sites[59–61]. Illumination of StilSwitch3 causes a loss of cholesterol from the antagonist-bound $A_{2A}R$ binding sites, whereas, for StilSwitch2 we observe less negative difference density over the cholesterol molecules (Supplementary Fig. 8). The loss of cholesterol from these sites indicates a movement of the $A_{2A}R$ away from its inactive, antagonist-bound state.

## Time-resolved synchrotron crystallography of ligand dissociation

Based on the results from the experiments under constant illumination, we concluded that ligand unbinding is more efficient when using StilSwitch3 and selected this variant for further analysis by time-resolved crystallography. For the collection of time-resolved serial crystallographic data, we used the recently established Kilohertz serial crystallography setup[62] at MaxIV (Supplementary Table 3). Due to the increased flux at this next-generation synchrotron source, we collected data with a temporal resolution of 2 ms over a window ranging up to 70 ms after the reaction was initiated with a laser pulse (Supplementary Fig. 9). To follow light-induced changes over time, we calculated a series of difference electron density maps ($F_o$(light)-$F_o$(dark)) each representing 2 ms in time and subjected them to Pearson correlation analysis[26,27] (Fig. 6A). The analysis revealed two major states, one ranging from ~2 to 40 ms and a second state contributing from 52 to 70 ms at the end of the measurement. Based on difference electron density maps calculated from the corresponding temporal ranges (Fig. 6B–D), the first state contains isomerized ligand in the *cis* conformation confirming our previous results in a time-resolved setup. In the case of the second state (Fig. 6E–G), near continuous negative density covers the position of the ligand, demonstrating that the transient *cis*-compound has left the binding pocket. Based on the difference density peaks observed, the two states of the receptor were modeled. Amino acids undergoing movement are clear from the q-weighted isomorphous difference maps, which offer an unbiased and highly sensitive view

https://doi.org/10.1038/s41467-024-55109-w

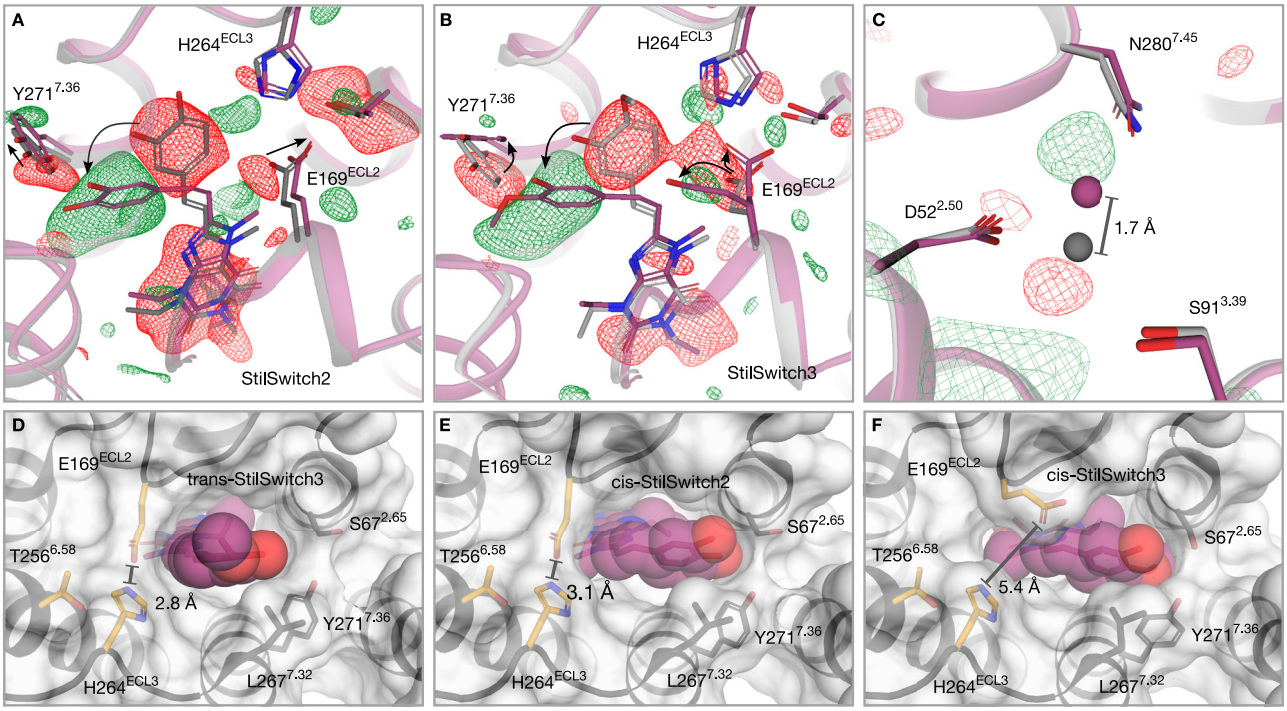


**Fig. 5 | Structural changes in the ligand binding pocket.** Changes observed in the $A_{2A}R$ after isomerization of StilSwitch2 (**A**) and StilSwitch3 (**B**). Dark state (gray) and light state (purple) models are displayed overlayed with isomorphous difference maps ($F_o$(light)-$F_o$(dark), red, negative and green, positive at 3.0 sigma) carved around the light-activated switch. **C** View of the allosteric sodium binding site showing movement of the sodium ion after illumination and isomerization of Switch3 (purple) relative to the dark state (gray). **D** Even in the presence of the trans conformation of our istradefylline derivatives, the $A_{2A}R$ ligand binding pocket is relatively open on the extracellular side. **E** In the case of Switch2, light activation widens the pocket but leaves the interaction between $E169^{ECL2}$ and $H264^{ECL3}$ intact. **F** In contrast the larger clash introduced by the extra methyl group has led to a shift of Switch3 towards the extracellular side and has widened the pocket by opening the interaction between $E169^{ECL2}$ and $H264^{ECL3}$.

into differences between two isomorphous structures (Fig. 6B, E). A lack of difference density is seen around the bRIL insertion protein (Fig. 6A), highlighting that changes throughout the protein are caused by photoswitch isomerization. However, this insertion likely also constrains the motion of TM5 and TM6, which see a drop in the volume of difference electron density towards the extracellular side (Fig. 6B, E).

Due to the low resolution of the extrapolated dataset at 52–70 ms, determining the position of side chains in the apo state remains difficult. Based on the appearance of negative densities over $E169^{ECL2}$ and $H264^{ECL3}$, it is clear that the salt bridge between these residues has been broken. $H264^{ECL3}$ moves away from the binding pocket along with ECL3, allowing $E169^{ECL2}$ to move flexibly and widen the opening of the binding pocket (Fig. 6D, G). In the binding pocket, additional difference densities suggest that after ligand dissociation, the space of the binding pocket is taken up by $Y271^{7.36}$ and $F168^{ECL2}$, residues which form important interactions with both bound agonizts and antagonists[21]. In both states, movements are not just constrained to the binding pocket and spread throughout the receptor (Fig. 6A, E), demonstrating that the designed photoswitch is a viable trigger to induce global conformational changes.

These results unequivocally demonstrate that ligand dissociation can be triggered by illumination of StilSwitch3 and monitored over time. However, the extent of the observed dynamics was somewhat unexpected. GPCRs are notoriously difficult to crystallize, often requiring thermostabilized mutants[63] or the incorporation of soluble fusion proteins[64]. Due to this limitation, we were unable to crystallize the wild-type $A_{2A}$ receptor. Instead, we employed a construct that combines a bRil fusion with thermostabilizing mutants to facilitate structure-based drug design starting from low-affinity ligands[65]. Although we reverted the A277S mutation due to its proximity to the binding pocket, this receptor variant is expected to have reduced affinity for agonizts, a bias toward inactive conformations, and overall lower conformational flexibility[66,67]. Despite these challenges, observations made in the thermostabilized receptor provide valuable insights into how photoinduced *trans*-to-*cis* isomerization alters ligand affinity. Our initial findings furthermore support previous suggestions regarding the changes occurring in the binding pocket during ligand dissociation[40,68], as well as the allosteric modulation by sodium[57,58] and cholesterol[60,61,69]. Collecting additional data at earlier time delays and at higher resolution will offer a clearer understanding of how, and to what extent, these conformational changes are propagated from the binding pocket.

Protein dynamics are essential for understanding biological functions, including signaling events triggered by ligand binding and dissociation. TRSX can capture dynamic data at atomic resolution across a wide temporal range, provided that well-ordered crystals and a suitable trigger system are available. In this study, we developed a photoswitch toolbox for the human adenosine $A_{2A}$ receptor and created a framework for evaluating photoswitches targeting other GPCRs. Our findings demonstrate how small structural changes impact ligand properties and the outcomes of serial crystallographic experiments.

Using photoswitches based on the Parkinson's drug istradefylline, we gained structural insights into how the binding pocket adapts to isomerizing ligands. The differences between StilSwitch2 and StilSwitch3 illustrate that ligand dissociation involves intermediate states, aligning with previous molecular dynamics simulations and models on the allosteric modulation of the receptor. Structural information from the transient *cis*-state and the apo-state reveals how photoswitch modifications influence ligand affinity post-photoisomerization, offering a molecular view into the dynamics of ligand dissociation.

https://doi.org/10.1038/s41467-024-55109-w

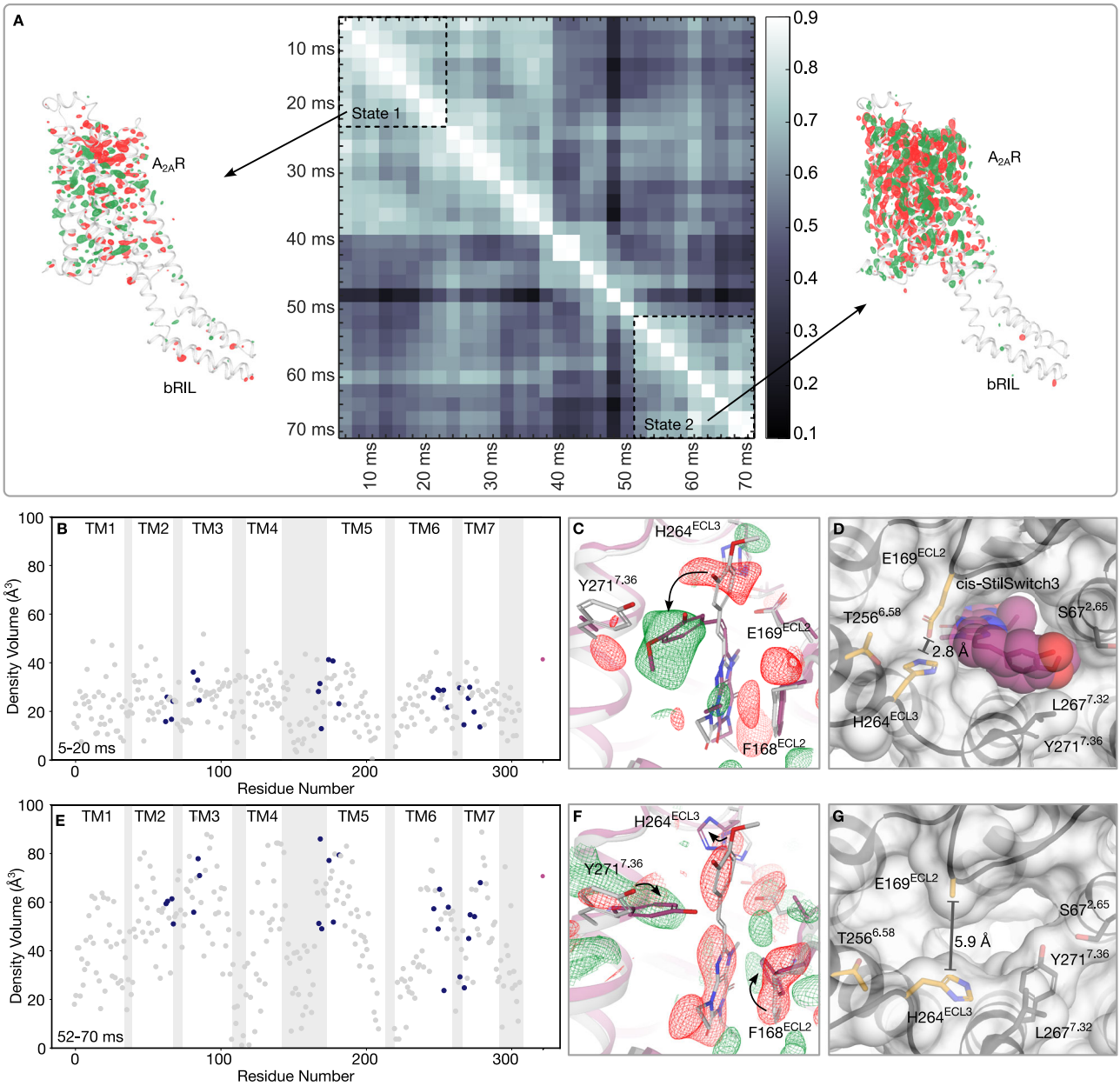


**Fig. 6 | Time-resolved serial synchrotron crystallography. A** Pearson correlation using overlapping data bins shows a clear shift in states between 40–50 ms after photoactivation. Q-weighted isomorphous difference electron density maps ($F_o$(light)-$F_o$(dark), red, negative and green, positive contoured at 3.0 sigma) show the distribution of residue displacement across the whole protein. **B**, **E** Plot showing the integrated absolute density volume at 3.0 sigma in a 2 Å radius around each residue in the $A_{2A}R$. Gray boxes show the position of loops along the $A_{2A}R$ protein and residues within 5 Å of the dark-state ligand are highlighted in blue. The density volume around the photoswitch is displayed in purple. **C**, **F** Model for changes observed in the binding pocket for state 1 (**C**) and state 2 (**F**). Dark state (gray) and light state (purple) models are displayed overlayed with q-weighted isomorphous difference maps ($F_o$(light)-$F_o$(dark), red, negative and green, positive at 3.0 sigma) carved around the highlighted residues and ligand. **D**, **G** View of the top of the $A_{2A}R$ binding pocket for the two states. Source data are provided as a source data file.

Our pioneering time-resolved measurements suggest that resolving intermediate states of GPCRs at high tempo-spatial resolution using optimized synchrotron beamlines or X-ray Free Electron Lasers is feasible. Although the current work relied on thermostabilized receptor variants, the efficient triggers we developed will facilitate the use of time as additional dimension for a deeper understanding of how ligands modulate signaling. Complementary techniques such as NMR, optical spectroscopy, or time-resolved cryo-EM could adapt the approach to further validate our results and provide a more complete view of GPCR behavior. This knowledge will advance structure-based drug design, ultimately leading to more precise and effective therapeutic strategies.

# Methods

## Photoswitch sources

Azobenzene-based derivatives of istradefylline were ordered custom-synthesized through Amel Pharmatech. These derivatives were synthesized based on a previously published scheme to synthesize 8-(phenylazo)xanthines via electrophilic coupling[70]. The purity of the resulting syntheses was then confirmed by Amel Pharmatech using $^1$H NMR in DMSO-d6 and liquid chromatography-mass spectroscopy. The stilbene-based photoswitches were ordered through the standard catalog of Tocris (istradefylline), MuseChem (StilSwitch1), and BOC Sciences (StilSwitch2, StilSwitch3, and StilSwitch4).

### Protein production

A thermostabilized construct of human $A_{2A}$ receptor, the $A_{2A}$-StaR2-$b_{RIL}$562 construct (with A277S revert mutation due to its proximity to the binding pocket)[65], was expressed using a FlashBAC system in *Trichoplusia ni* Hi5 cells. Cells were grown at 27 °C with constant shaking in Sf900 II media to a cell density of $4 \times 10^6$ ml$^{-1}$. Following bacmid infection using 2.5% VOI, cells were incubated for 48 h before harvesting.

Membrane preparation and protein purification were carried out as previously described[41], without the addition of ligand to buffers during purification so that protein could be purified in an apo state and used for experiments with different ligands. Cholesteryl hemisuccinate (CHS) was also added to buffers during the protein purification steps at a concentration of 0.1% (w/v) during membrane solubilization, and 0.002% (w/v) during affinity purification and SEC.

### Thermal shift assay

To monitor protein unfolding, 7-diethylamino-3-(4′-Maleimidylphenyl)-4-methylcoumarin (CPM) was used at a final concentration of 18.6 mM. Samples were incubated on ice for 30 min with 1.66 µM protein and 0.1 mM photoswitch in buffer containing 40 mM Tris pH 7.5, 250 mM NaCl, 0.15% DM, 0.002% CHS, and 5% glycerol. A 365 nm diode (ThorLabs) at 0.7 A was used to illuminate samples for varying amounts of time. Melting curves from 25 to 95 °C were collected using a RotoGene qPCR machine, with steps of 1 °C/4 s. To ensure that illumination itself had no effect on protein stability, a control experiment with no ligand was carried out, in which samples without ligand were subject to the same illumination conditions as photoswitch samples. From this, no large change in melting temperature was observed (+0.12 ± 0.04 °C calculated with 95% confidence intervals) and it was concluded that illumination alone has a negligible effect on protein stability. Unfortunately, the absorption of the azobenzene-based switches interfered with the assay, preventing the collection of thermal shift data.

### UV-Vis spectroscopy

Absorbance spectra were measured using a Shimadzu UV 2401PC spectrophotometer before and after 60 s of illumination with a 365 nm diode (Thorlabs), with a measured power of 1.9 mW at the sample position. Photoswitches were diluted to 25 mM in buffer containing 40 mM Tris pH 7.5, 200 mM NaCl, 0.15% DM, 0.002% CHS, 1% DMSO. For protein-bound measurements, ligands were incubated for 10 min with the protein, using a concentration of protein calculated to ensure at least 98% of ligand would be bound to protein[71]. To compare data between ligands, data were normalized to the absorbance of the trans peak for the dark spectra of the respective ligands.

Before the ultrafast measurements steady-state absorption spectra and illumination experiments were performed in acetonitrile and buffer for StilSwitch1-4 with a standard spectrophotometer (Specord S600, Analytik Jena). The photostationary state was achieved with a LED (ThorLabs M340L4). The steady-state fluorescence spectra were recorded with a FP-8500 spectrofluorometer (Jasco, Groß-Umstadt, Germany).

### Ultrafast spectroscopy

Ultrafast transient absorption measurements were performed with a homebuilt pump-probe setup. The fs-laser system includes a Ti:Sapphire oscillator (Mai Tai SPNSI, Spectra-Physics), which seeds an amplifier (Spitfire Ace100F1K, Spectra-Physics). The amplifier is pumped by a Nd:YLF laser (Empower 45, Spectra-Physics). The resulting laser pulses had 110 fs temporal width, centered at 800 nm, and a repetition rate of 1 kHz. The pump pulse was generated with a homebuilt two-stage NOPA (620 nm) followed by a SFG (350 nm). The pump pulses had an energy of 75 nJ/pulse. White light continuum was used to probe the dynamics. The continuum was generated by focusing the 800 nm fundamental into a $CaF_2$ crystal (3 mm). The probe pulses were analyzed by a spectrometer (AvaSpec-ULS2048CL-EVO-RS, Avantes). The sample was prepared in a 1 mm quartz cuvette, which was continuously moved to avoid photodegradation. For all samples, the OD was fixed around 0.7 OD and was illuminated with a LED (Thorlabs: M280L6). For measurements of StilSwitch3 with protein, an excess of protein was used to ensure at least 98% of the ligand would be bound to protein so that contributions of the unbound form of the ligand could be minimized[71]. Protein was then incubated with the ligand for 10 min prior to its use to ensure a binding equilibrium had been reached.

### Crystallization

For conventional cryo-crystallography, ligands were soaked into $A_{2A}$-$b_{RIL}$562-Theophylline crystals prepared using the previously described method[65]. Resulting crystals were 40–70 mm long swallow-tailed plates. Ligands were soaked into crystals for 1 h using mother liquor containing 1 mM of added ligand. In the cases of AzoSwitch1 and AzoSwitch3, additional DMSO was added to the soaking buffer (to a maximum of 2% to avoid effects on the LCP and protein crystals) to help improve ligand solubility. However, no improvement was observed.

The $A_{2A}$ receptor was crystallized directly with StilSwitch2, StilSwitch3, and StilSwitch4 for serial data collection. A modified well-based LCP crystallization[72] using EasyXtal plates (Molecular Dimensions) was used for large-scale crystal preparation. This method allowed for the reproducible crystallization of the large amounts of LCP required for serial crystallographic experiments using a viscous injector setup. 15 µL of LCP was added to wells containing 0.1 M NaK phosphate pH 5.85, 27–30% PEG 500 MME, 0.2 M NaSCN, 0.4 mM photoswitch at a 1:35 LCP: mother liquor ratio. Crystals appeared after 2–3 days and were fully grown after 2 weeks. Crystal-laden LCP were pooled into a 500 mL Hamilton syringe, with a small amount of mother liquor, after 3 weeks following setup. Incubation of crystals in the plates for longer amounts of time resulted in the formation of a sponge phase, which is both harder to harvest and jet. To prepare samples for jetting, crystal-laden LCP was pooled and mixed with up to 5% monoolein until a jetting consistency was reached.

### Cryo crystallographic data collection and processing

Conventional cryo-crystallography data were taken at the Swiss Light Source (SLS) at X06SA (Istradefylline, AzoSwitch2, StilSwitch1, StilSwitch2) and X10SA (StilSwitch3, StilSwitch4) using an Eiger 16 M detector. Data were collected with an oscillation of 0.2° and an exposure of 0.04 s per frame at a 180° rotation range. Automated data processing was used during data collection[73]. Aimless from the CCP4 suite of programs[74] was then used to merge and scale data. Analysis of $R_{merge}$ and relative B factors against the image number was used to identify and removed bad batches from the dataset[75]. In some cases, data from multiple crystals were merged to improve data quality: StilSwitch1, 3 crystals; StilSwitch2, 9 crystals; StilSwitch3, 6 crystals.

### Steady-state serial data collection and processing

Steady-state data were collected using the X06SA beamline (Swiss Light Source). Samples were delivered to the intersection point of the X-ray beam and laser diode with a high-viscosity extruder through a 75 µm glass capillary nozzle at a speed of 1000 µm s$^{-1}$. Data were collected using a Jungfrau detector at 250 Hz with an X-ray beam focused to 25 × 10 µm (horizontal x vertical) FWHM at 12.4 keV. At the flux of $1.5 \times 10^{12}$ photons s$^{-1}$, each 4 ms exposure delivers a dose of about 7 kGy as estimated using Raddose 3D[76], well below the assumed room-temperature radiation limit of 300 kGy[77].

A 405 nm laser diode (RLDE405M-20-5 Roithner Lasertechnik) was used for illumination and was focused to 75 × 100 µm (horizontal x

vertical) with a measured power of 2.5 mW on the LCP jet. In this way constant illumination allowed for the collection of steady state datasets of roughly 50 ms light exposure.

Collected data were processed with Crystfel 0.9.1[78,79], using peakfinder8 for peak detection, and XGANDALF[80] and MOSFLM for peak integration, with the settings: *--threshold = 6 --min-snr = 5 --min-pix-count = 2*. Data was merged and scaled using partialator with model unity.

Isomorphous difference maps and extrapolated maps were created with Xtrapol8[81], using q-weighting with data ranging from 2.8 to 20.0 Å for StilSwitch2, and 3.0 to 20.0 Å for StilSwitch3. $R_{iso}$ and $CC_{iso}$ values calculated during this process can be found in Supplementary table 2. qFextr maps were produced from extrapolated structure factor amplitudes calculated using the truncate option, in which negative reflections are dealt with using the French–Wilson algorithm. For extrapolated map calculation, reference pdb files not containing ligands were used. Occupancy determination was carried out using the difference-map method and was confirmed by manual evaluation of the calculated maps. An occupancy of 0.4 for both StilSwitch2 and StilSwitch3 was used.

### Structure determination and refinement

Molecular replacement with the search model 5MZJ was used to solve cryo structures, for room temperature serial data, the search model 6S0L was used. Models were then refined with iterative cycles of phenix.refine[82] and manual refinement with coot. Ligand restraints were generated using the Grade web server[83].

### Time-resolved serial data collection and processing

Data were collected at the BioMAX beamline at MaxIV using an Eiger 16 M detector. The X-ray beam was focused to $20 \times 5\ \mu m^2$ (horizontal x vertical) FWHM with a photon energy of 11 keV. For reaction initiation, a 2 ms pulse from a 100 mW 400 nm laser (RLDE405M-20-5 Roithner Lasertechnik) focused to $80 \times 200\ \mu m$ FWHM was offset by ~30 μm from the X-ray focal point. For time-resolved data collection, samples were extruded using a high-viscosity injector[84,85] at a speed of $1000\ \mu m\ s^{-1}$. Data were collected at 500 Hz resulting in a distance of 2 μm between exposures. At the flux of $5 \times 10^{12}$ photons $s^{-1}$, each 2 ms exposure delivered a dose of about 30 kGy as calculated using Raddose 3D[76], remaining well within commonly assumed room-temperature radiation limits[77]. The chosen balance between dose and extrusion speed allowed to efficiently scan microcrystals[54] while making optimal use of the higher flux generated at this next-generation synchrotron source. Collected data were processed with Crystfel 0.10.2[78,79], using peakfinder8 for peak detection, and XGANDALF[80], MOSFLM, and DirAx for peak integration, with the settings: *--threshold = 10 –min-snr = 5.4, --min-pix-count = 1*. Data was merged and scaled using partialator with the model unity. Mtz files were created with the CCP4 suite[74] and isomorphous difference maps for pearson correlation analysis were computed with PHENIX[86,87].

### Pearson correlation analysis of time-resolved data

$F_o$(light)-$F_o$(dark) difference maps were analyzed for similarities in difference density peaks larger than 3.0 sigma, 1.5 Å surrounding the photoswitch, using a pairwise Pearson correlation of all time points, as has been described previously[13,55]. This enabled the identification of two states. Patterns from datasets representing these states were merged, resulting in the creation of a dataset from 5 to 20 ms (with 41,593 patterns) and a dataset from 52 to 70 ms with 41,471 patterns. These datasets were scaled together with a similarly sized (41,943 patterns) dark dataset using the --custom-split option in partialator. Xtrapol8 was then used to calculate q-weighted $F_o$(light)-$F_o$(dark) maps with a 3.0 Å and 3.5 Å resolution cutoff for the 5–20 ms and 52–70 ms datasets respectively.

### Reporting summary

Further information on research design is available in the Nature Portfolio Reporting Summary linked to this article.

## Data availability

Coordinates and structure factors have been deposited in the PDB database under accession codes 8RW0 (for the istradefylline cryo-structure), 8RW4 (for the AzoSwitch2 cryo-structure), 8RW7 (for the StilSwitch1 cryo-structure), 8RWC (for the StilSwitch2 cryo-structure), 8RWD (for the StilSwitch3 cryo-structure), 8RWE (for the StilSwitch4 cryo-structure), 8RWH (for the StilSwitch2 steady state dark structure), 8RWI (for the StilSwitch2 steady state light structure), 8RVW (for the StilSwitch3 steady state dark structure), and 8RWX (for the StilSwitch3 steady state light structure). Source data for plots are provided with this paper. Source data are provided with this paper.

## References


1. Schulz, E. C., Yorke, B. A., Pearson, A. R. & Mehrabi, P. Best practices for time-resolved serial synchrotron crystallography. *Acta Cryst.* **D78**, 14–29 (2022).
2. Standfuss, J. Membrane protein dynamics studied by X-ray lasers - or why only time will tell. *Curr. Opin. Struct. Biol.* **57**, 63–71 (2019).
3. Brändén, G. & Neutze, R. Advances and challenges in time-resolved macromolecular crystallography. *Science* **373**, eaba0954 (2021).
4. Khusainov, G., Standfuss, J. & Weinert, T. The time revolution in macromolecular crystallography. *Struct. Dyn.* **11**, 020901 (2024).
5. Monteiro, D. C. F., Amoah, E., Rogers, C. & Pearson, A. R. Using photocaging for fast time-resolved structural biology studies. *Acta Cryst.* **D77**, 1218–1232 (2021).
6. Hoorens, M. W. H. & Szymanski, W. Reversible, Spatial and temporal control over protein activity using light. *Trends Biochem. Sci.* **43**, 567–575 (2018).
7. Velema, W. A., Szymanski, W. & Feringa, B. L. Photopharmacology: beyond proof of principle. *J. Am. Chem. Soc.* **136**, 2178–2191 (2014).
8. Broichhagen, J., Frank, J. A. & Trauner, D. A roadmap to success in photopharmacology. *Acc. Chem. Res.* **48**, 1947–1960 (2015).
9. Sheldon, J. E., Dcona, M. M., Lyons, C. E., Hackett, J. C. & Hartman, M. C. T. Photoswitchable anticancer activity via trans–cis isomerization of a combretastatin A-4 analog. *Org. Biomol. Chem.* **14**, 40–49 (2016).
10. Jerca, F. A., Jerca, V. V. & Hoogenboom, R. Advances and opportunities in the exciting world of azobenzenes. *Nat. Rev. Chem.* **6**, 51–69 (2022).
11. Weinert, T. et al. Serial millisecond crystallography for routine room-temperature structure determination at synchrotrons. *Nat. Commun.* **8**, 1–11 (2017).
12. Weinert T. et al. Direct observation of coherent azobenzene photochemistry. https://doi.org/10.21203/rs.3.rs-3490897/v1 (2023).
13. Wranik, M. et al. Watching the release of a photopharmacological drug from tubulin using time-resolved serial crystallography. *Nat. Commun.* **14**, 1–12 (2023).
14. Irie, M., Fukaminato, T., Sasaki, T., Tamai, N. & Kawai, T. Organic chemistry: a digital fluorescent molecular photoswitch. *Nature* **420**, 759–760 (2002).
15. Browne, W. R. & Feringa, B. L. Making molecular machines work. *Nat. Nanotechnol.* **1**, 25–35 (2006).
16. Bozovic, O., Jankovic, B. & Hamm, P. Using azobenzene photocontrol to set proteins in motion. *Nat. Rev. Chem.* **6**, 112–124 (2022).
17. Dumaze, A. et al. Optical control of adenosine A2A receptor using istradefylline photosensitivity. *ACS Chem. Neurosci.* **15**, 645–655 (2024).

18. Araya, T. et al. Crystal structure reveals the binding mode and selectivity of a photoswitchable ligand for the adenosine A2A receptor. *Biochem. Biophys. Res. Commun.* **695**, 149393 (2024).
19. Congreve, M., De Graaf, C., Swain, N. A. & Tate, C. G. Impact of GPCR structures on drug discovery. *Cell* **181**, 81–91 (2020).
20. Zhou, Q. et al. Common activation mechanism of class A GPCRs. *eLife* **8**, e50279 (2019).
21. Carpenter, B. & Lebon, G. Human adenosine A2A receptor: molecular mechanism of ligand binding and activation. *Front. Pharmacol.* **8**, 898–898 (2017).
22. Weis, W. I. & Kobilka, B. K. The molecular basis of G protein-coupled receptor activation. *Annu. Rev. Biochem.* **87**, 897–919 (2018).
23. Gusach, A. et al. Beyond structure: emerging approaches to study GPCR dynamics. *Curr. Opin. Struct. Biol.* **63**, 18–25 (2020).
24. Bostock, M. J., ASolt, A. S. & Nietlispach, D. The role of NMR spectroscopy in mapping the conforrmational landscape of GPCRs. *Curr. Opin. Struct. Biol.* **57**, 145–156 (2019).
25. Chavez-Abiega, S., Goedhart, J. & Bruggeman, F. J. Physical biology of GPCR signalling dynamics inferred from fluorescence spectroscopy and imaging. *Curr. Opin. Struct. Biol.* **55**, 204–211 (2019).
26. Huang, Z. L. et al. Adenosine A2A, but not A1, receptors mediate the arousal effect of caffeine. *Nat. Neurosci.* **8**, 858–859 (2005).
27. Mori, A. How do adenosine A2A receptors regulate motor function? *Parkinsonism Relat. Disord.* **80**, 13–20 (2020).
28. Real, J. I., Simões, A. P., Cunha, R. A., Ferreira, S. G. & Rial, D. Adenosine A2A receptors modulate the dopamine D2 receptor-mediated inhibition of synaptic transmission in the mouse prefrontal cortex. *Eur. J. Neurosci.* **47**, 1127–1134 (2018).
29. Cieślak, M., Komoszyński, M. & Wojtczak, A. Adenosine A2A receptors in Parkinson's disease treatment. *Purinergic Signal.* **4**, 305–312 (2008).
30. Dungo, R. & Deeks, E. D. Istradefylline: first global approval. *Drugs* **73**, 875–882 (2013).
31. Jaakola, V. P. et al. The 2.6 angstrom crystal structure of a human A2A adenosine receptor bound to an antagonist. *Science* **322**, 1211–1217 (2008).
32. Carpenter, B., Nehme, R., Warne, T., Leslie, A. G. & Tate, C. G. Structure of the adenosine A2A receptor bound to an engineered G protein. *Nature* **536**, 104–107 (2016).
33. Lebon, G. et al. Agonist-bound adenosine A2A receptor structures reveal common features of GPCR activation. *Nature* **474**, 521–525 (2011).
34. Wang, Y. et al. Design, synthesis, and biological activity studies of istradefylline derivatives based on adenine as A2A receptor antagonists. *ACS Omega* **6**, 4386–4394 (2021).
35. Xu, H. et al. Investigation of photostability of istradefylline aqueous solution. *Chem. Sel.* **5**, 2337–2341 (2020).
36. Nonaka, Y. et al. Communications to the editor photoisomerization of a potent and selective adenosine A2 antagonist, (E)-l, 3-Dipropy 1-8-(3,4-dimethoxy styryl)-7-methylxanthine. *J. Med. Chem.* **36**, 38–38 (1993).
37. Ballesteros, J. A. & Weinstein, H. Integrated methods for the construction of three-dimensional models and computational probing of structure-function relations in g protein-coupled receptors. *Methods Neurosci.* **25**, 366–428 (1995).
38. Neukirch, A. J. et al. Nonadiabatic ensemble simulations of cis-stilbene and cis-azobenzene photoisomerization. *J. Chem. Theory Comput.* **10**, 23–23 (2014).
39. Cheng, R. K. Y. et al. Structures of human A1 and A2A adenosine receptors with xanthines reveal determinants of selectivity. *Structure* **25**, 1275–1285.e1274 (2017).
40. Guo, D. et al. Molecular basis of ligand dissociation from the adenosine A2A receptor. *Mol. Pharmacol.* **89**, 485–491 (2016).
41. Segala, E. et al. Controlling the dissociation of ligands from the adenosine A 2A receptor through modulation of salt bridge strength. *J. Med. Chem.* **59**, 6470–6479 (2016).
42. Zhang, X., Stevens, R. C. & Xu, F. The importance of ligands for G protein-coupled receptor stability. *Trends Biochem. Sci.* **40**, 79–87 (2015).
43. Alexandrov, A. I., Mileni, M., Chien, E. Y. T., Hanson, M. A. & Stevens, R. C. Microscale fluorescent thermal stability assay for membrane proteins. *Structure* **16**, 351–359 (2008).
44. Liang, R. & Bakhtiiari, A. Effects of enzyme-ligand interactions on the photoisomerization of a light-regulated chemotherapeutic drug. *J. Phys. Chem. B* **126**, 2382–2393 (2022).
45. Gilabert, E., Lapouyade, R. & Rullière, C. Dual fluorescence in trans-4-dimethylamino-4′-cyanostilbene revealed by picosecond time-resolved spectroscopy: a possible new "TICT" compound. *Chem. Phys. Lett.* **145**, 262–268 (1988).
46. Abraham, E., Oberlé, J., Jonusauskas, G., Lapouyade, R. & Rullière, C. Photophysics of 4-dimethylamino 4′-cyanostilbene and model compounds: dual excited states revealed by sub-picosecond transient absorption and Kerr ellipsometry. *Chem. Phys.* **214**, 409–423 (1997).
47. Oberlé, J., Jonusauskas, G., Abraham, E., Lapouyade, R. & Rullière, C. Time-resolved charge transfer in "push-pull" stilbenes. *BCSJ* **75**, 1041–1047 (2002).
48. Sen, RafiqS. Dielectric controlled excited state relaxation pathways of a representative push-pull stilbene: a mechanistic study using femtosecond fluorescence up-conversion technique. *J. Chem. Phys.* **138**, 84308–84308 (2013).
49. Singh, C., Ghosh, R., Mondal, J. A. & Palit, D. K. Excited state dynamics of a push-pull stilbene: a femtosecond transient absorption spectroscopic study. *J. Photochem. Photobiol. A Chem.* **263**, 50–60 (2013).
50. Wang, R. et al. Structural investigation of azobenzene-containing self-assembled monolayer films. *J. Electroanal. Chem.* **438**, 213–219 (1997).
51. Kusukawa, T. & Fujita, M. Ship-in-a-bottle' formation of stable hydrophobic dimers of cis- azobenzene and -stilbene derivatives in a self-assembled coordination nanocage. *J. Am. Chem. Soc.* **121**, 1397–1398 (1999).
52. Lorenz, L., Kusebauch, U., Moroder, L. & Wachtveitl, J. Temperature- and photocontrolled unfolding/folding of a triple-helical azobenzene-stapled collagen peptide monitored by infrared spectroscopy. *ChemPhysChem* **17**, 1314–1320 (2016).
53. Slavov, C. et al. Twist and return-induced ring strain triggers quick relaxation of a (Z)-stabilized cyclobisazobenzene. *J. Phys. Chem. Lett.* **9**, 4776–4781 (2018).
54. Weinert, T. et al. Proton uptake mechanism in bacteriorhodopsin captured by serial synchrotron crystallography. *Science* **365**, 61–65 (2019).
55. Skopintsev, P. et al. Femtosecond-to-millisecond structural changes in a light-driven sodium pump. *Nature* **583**, 314–318 (2020).
56. Mous, S. et al. Dynamics and mechanism of a light-driven chloride pump. *Science* **375**, 845–851 (2022).
57. Katritch, V. et al. Allosteric sodium in class A GPCR signaling. *Trends Biochem. Sci.* **39**, 233–244 (2014).
58. Liu, W. et al. Structural basis for allosteric regulation of GPCRs by sodium ions. *Science* **337**, 232–236 (2012).
59. Tzortzini E., Corey R. A., Kolocouris A. Comparative study of receptor-, receptor state-, and membrane-dependent cholesterol binding sites in $A_{2A}$ and $A_1$ adenosine receptors using coarse-grained molecular dynamics simulations. *J. Chem. Inf. Model.* **63**, 928–949 (2023).
60. Huang, S. K. et al. Allosteric modulation of the adenosine A2A receptor by cholesterol. *eLife* **11**, e73901 (2022).

61. Lovera, S., Cuzzolin, A., Kelm, S., De Fabritiis, G. & Sands, Z. A. Reconstruction of apo A2A receptor activation pathways reveal ligand-competent intermediates and state-dependent cholesterol hotspots. *Sci. Rep.* **9**, 1–10 (2019).
62. Leonarski, F. et al. Kilohertz serial crystallography with the JUNGFRAU detector at a fourth-generation synchrotron source. *IUCrJ* **10**, 729–737 (2023).
63. Tate, C. G. A crystal clear solution for determining G-protein-coupled receptor structures. *Trends Biochem. Sci.* **37**, 343–352 (2012).
64. Chun, E. et al. Fusion partner toolchest for the stabilization and crystallization of g protein-coupled receptors. *Structure* **20**, 967–976 (2012).
65. Rucktooa, P. et al. Towards high throughput GPCR crystallography: in Meso soaking of Adenosine A2A Receptor crystals. *Sci. Rep.* **8**, 1–7 (2018).
66. Vaidehi, N., Grisshammer, R. & Tate, C. G. How can mutations thermostabilze g-protein-coupled receptors? *Trends Pharmacol. Sci.* **37**, 37–46 (2016).
67. Doré, A. S. et al. Structure of the adenosine A2A receptor in complex with ZM241385 and the xanthines XAC and caffeine. *Structure* **19**, 1283–1283 (2011).
68. Segala, E. et al. Controlling the dissociation of ligands from the adenosine A2A receptor through modulation of salt bridge strength. *J. Med. Chem.* **59**, 6470–6479 (2016).
69. Tzortzini, E., Corey, R. A. & Kolocouris, A. Comparative study of receptor-, receptor state-, and membrane-dependent cholesterol binding sites in A2A and A1 adenosine receptors using coarse-grained molecular dynamics simulations. *J. Chem. Inf. Model.* **63**, 928–949 (2023).
70. Müller, C. E. et al. Aza-analogs of 8-styrylxanthines as A2A-adenosine receptor antagonists. *Arch. Pharm.* **330**, 181–189 (1997).
71. Jarmoskaite, I., Alsadhan, I., Vaidyanathan, P. P. & Herschlag, D. How to measure and evaluate binding affinities. *eLife* **9**, 1–34 (2020).
72. Andersson, R. et al. Well-based crystallization of lipidic cubic phase microcrystals for serial X-ray crystallography experiments. *Acta Cryst.* **D75**, 937–946 (2019).
73. Wojdyla J. A. et al. DA+ data acquisition and analysis software at the Swiss light source macromolecular crystallography beamlines. *J. Synchrotron Radiat.* **25**, 293–303 (2018).
74. Winn, M. D. et al. Overview of the CCP4 suite and current developments. *Acta Crystallogr D. Biol. Crystallogr* **67**, 235–242 (2011).
75. Evans, P. R. & Murshudov, G. N. How good are my data and what is th resolution? *Acta Crystallogr D. Biol. Crystallogr* **69**, 1204–1214 (2013).
76. Zeldin, O. B., Gerstel, M. & Garman, E. F. RADDOSE-3D: time- and space-resolved modelling of dose in macromolecular crystallography. *J. Appl. Crystallogr.* **46**, 1225–12300 (2013).
77. Holton, J. M. A beginner's guide to radiation damage. *J. Synchrotron Radiat.* **16**, 133–142 (2009).
78. White, T. A. et al. CrystFEL: a software suite for snapshot serial crystallography. *J. Appl. Crystallogr.* **45**, 335–341 (2012).
79. White, T. A. et al. Recent developments in CrystFEL. *J. Appl. Cryst.* **49**, 680–689 (2016).
80. Gevorkov, Y. et al. XGANDALF – extended gradient descent algorithm for lattice finding. *Acta Cryst.* **A75**, 694–704 (2019).
81. De Zitter, E., Coquelle, N., Oeser, P., Barends, T. R. M. & Colletier, J.-P. Xtrapol8 enables automatic elucidation of low-occupancy intermediate-states in crystallographic studies. *Commun. Biol.* **5**, 1–11 (2022).
82. Afonine, P. V. et al. Towards automated crystallographic structure refinement with phenix.refine. *Acta Cryst.* **D68**, 352–367 (2012).
83. Smart O. S. et al. Grade.). Global Phasing Ltd. (2013).
84. Weierstall, U. et al. Lipidic cubic phase injector facilitates membrane protein serial femtosecond crystallography. *Nat. Commun.* **5**, 1–6 (2014).
85. Shilova, A. et al. Current status and future opportunities for serial crystallography at MAX IV Laboratory. *J. Synchrotron Radiat.* **27**, 1095–1102 (2020).
86. Pražnikar, J., Afonine, P. V., Guncar, G., Adams, P. D. & Turk, D. Averaged kick maps: less noise, more signal... and probably less bias. *Acta Crystallogr D. Biol. Crystallogr* **65**, 921–931 (2009).
87. Adams, P. D. et al. PHENIX: building new software for automated crystallography structure determination. *Acta Crystallogr D. Biol. Crystallogr* **58**, 1948–1954 (2002).


## Acknowledgements

We are grateful for the excellent support from the PSI Crystallization Facility and the Macromolecular Crystallography group during growing and testing of crystals at the Swiss Light Source. The Biomolecular Structure and Mechanism Program of the Life Science Zürich Graduate School is acknowledged for the excellent academic framework provided to our students. Swiss National Science Foundation Project Grants 310030_197674 (to T.W.) and 310030_207462 (J.S.). Swiss Innovation Agency Innosuisse Grant 42711.1 IP-LS (to M.H. and J.S.). Swiss National Science Foundation Sinergia Grant CRSII5_213507 (J.S.). Swiss Nanoscience Institute SNI #1904 (M.C.), German Research Foundation, Project WA 1850/4-3 (C.S., J.W.). German Research Foundation, GRK 1986, CLiC: Complex Scenarios of Light-Control (J.W.)

## Author contributions

Conceptualization: J.S., W.N., and M.H. Methodology: H.G., and T.S. Investigation: H.G., T.S., Q.B., M.T., A.B., F.A., C.S., Y.K., R.S., M.W., G.K., M.C., D.K., J.N., A.G., R.C., T.W., F.L., F.D., M.K., and J.S. Visualization: H.G., and T.S. Supervision: J.S., M.H., and J.W. Writing—original draft: H.G., T.S., and J.S. Writing—review & editing: H.G., T.S., J.S., T.W., M.K., Q.B., R.C., M.C., Y.K., and M.T.

## Competing interests

Authors M.T., A.B., F.A., R.C., W.N., and M.H. are employees of LeadXpro Biotech A.G., a company offering services for GPCR drug design and developing own lead compounds. The other authors declare no competing interests.

## Additional information

**Supplementary information** The online version contains supplementary material available at https://doi.org/10.1038/s41467-024-55109-w.

**Correspondence** and requests for materials should be addressed to Joerg Standfuss.

**Peer review information** *Nature Communications* thanks Kenneth Jacobson and the other, anonymous, reviewer(s) for their contribution to the peer review of this work. A peer review file is available.